## Electronic Supplementary Information

**Supplementary Material 1.** Real-time videos of the responses of the droplets against UV irradiation on bare (Movies S1 (a) and (b)), PVA-coated (Movies S1 (c) and (d)) and JALS204-coated substrates (Movies S1 (e) and (f)). Temperature was set to be ~60 °C. (a), (c) and (e) are the time evolutions just after the UV irradiation, and (b), (d) and (f) just after stopping the irradiation.

**Supplementary Material 2.** Detail about trial functions of Eqs. (3), (2) and (4). Eq. (3) was designed on the basis of the schematic illustrations of Fig. S1. For simplicity, we discuss the case of $\phi_0 = 0$, where the director aligns along x direction at xy-plane ($z = 0$). In this situation, the director field was assumed as,

$$n_x = \cos\theta_n \cos\phi_n$$
$$n_y = -\cos\theta_n \sin\phi_n \quad (S1),$$
$$n_z = -\sin\theta_n$$

where

$$\theta_n = \frac{\alpha zx}{hR}$$
$$\phi_n = \frac{\beta zxy}{hR^2} \quad (S2).$$

Owing to the strong planar anchoring at $z = 0$, the director basically aligns along $x$ direction, while it is slightly modulated owing to the weak anchoring at the air-LC interface. $\theta_n$ indicates the tilt angle, and $\phi_n$ the azimuthal angle, both of which are set to be zero when the director aligns along $x$ direction. Since $\theta_n$ should be zero for $x = 0$, or $z = 0$ owing to the anchoring conditions (see, Fig. S2(a)), it was assumed to be proportional to $x$ and $z$ as shown in Eq. (S2). Similarly, since $\phi_n$ should be zero for $x = 0$, $y = 0$, or $z = 0$, it was set to be proportional to $x, y$ and $z$. The strength of the modulations are controlled by $\alpha$ and $\beta$, whose physical meanings are schematically illustrated in Figs. S2(a) and (b). They are the extrapolated value of the tilt and the azimuthal angles at the position of $(R, 0, h)$ and $(R, R, h)$, respectively.

Generalizing the discussion above into the case of $\phi_0 \neq 0$, and showing the director in the radial

coordinate, we obtain Eq. (3). The physical meaning of $\alpha$ in Eq. (2) can also be described with similar way.

The azimuthal angle distribution in Eq. (2) was designed on the basis of the schematic illustrations of Fig. S2. Here, for simplicity, we only focus on the director field in $xy$-plane ($z=0$) and discuss the case of $\phi_0 = 0$, where the two defect lines lie in $xz$-plane. Now, the lines are described by the two points (cross symbols in Fig. S2). As shown by the red circle in Fig. S2, we can draw circles with the defect points passing through, and any point in the droplet should be in one of such circles.

As shown in Fig. S2, $\phi_n$ is the azimuthal angle of the director, which is a function of the coordinates $x$ and $y$ ($\phi_n(x,y)$). We consider how $\phi_n$ should change along the orbital of the red circle, to design the trial function showing the director field as illustrated in Fig. 4(b"). For simplicity, we restrict the discussion to the first quadrant ($x>0, y>0$). When the orbital cross the y axis, $\phi_n$ should be 0, which can be written as $\phi_n(0,y_e)=0$. On the other hand, since the defect point has $+1/2$ topological charge, $\phi_n$ at the point can be described as $\phi_n(R_d,0)=(\phi_d-\pi)/2$, where physical meaning of $\phi_d$ is shown in Fig. S2. Thus, along the orbital of the red circle, $\phi_n$ should gradually change from 0 to $(\phi_d-\pi)/2$. As one way, we can satisfy this condition with setting $\phi_n = -\phi_p/2$, where the parameter $\phi_p$ is defined as shown in Fig. S2. From elemental geometric calculations, we obtain $\phi_d$ and $\phi_p$ as

$$
\begin{aligned}
\tan\phi_d &= \frac{2R_d r \sin\phi}{r^2 - R_d^2} \\
\tan\phi_p &= \frac{r\cos\phi\sin\phi_d}{r\sin\phi\sin\phi_d - R_d\cos\phi_d}
\end{aligned}
, \quad (S3)
$$

where $r=\sqrt{x^2+y^2}$ and $\phi = \arctan(y/x)$.

Repeating this discussion in the second, third, and fourth quadrants, and generalizing it into the case of $\phi_0 \neq 0$, we obtain the equations below Eq. (2).

Eq. (4) was designed on the basis of the schematic illustrations of Fig. S3. In the radial coordinate, the director field is assumed as,

$$n_r = \sin\theta_n \cos\phi_n$$
$$n_\phi = -\sin\theta_n \sin\phi_n \quad \text{(S4)},$$
$$n_z = -\cos\theta_n$$

where

$$\theta_n = \frac{\pi z}{2\pi}$$
$$\phi_n = \frac{\beta(R-r)}{R} \quad \text{(S5)}.$$

$\theta_n$ indicates the polar angle of the director. Because of the homeotropic anchoring at the substrate and the planar anchoring at the air-LC interface, $\theta_n$ might be zero at $z=0$ and $\pi/2$ at $z=R$. Thus, we assumed $\theta_n$ would be proportional to $z$ as shown in Eq. (S5) for simplicity. The definition of $\phi_n$ is schematically illustrated Fig. (S3), and $\phi-\phi_n$ indicates the azimuthal angle of the director. The director field shows pure splay deformation when $\phi_n=0$, while bend when $\phi_n=\pi/2$. We assumed that $\phi_n$ would be extrapolated to be zero at $r=R$, and proportional to $r$ with the slope of $\beta/R$. Hence, in Eq. (S5), $\beta$ indicates the extrapolated value of $\phi_n$ at $r=0$, where defect line is induced.
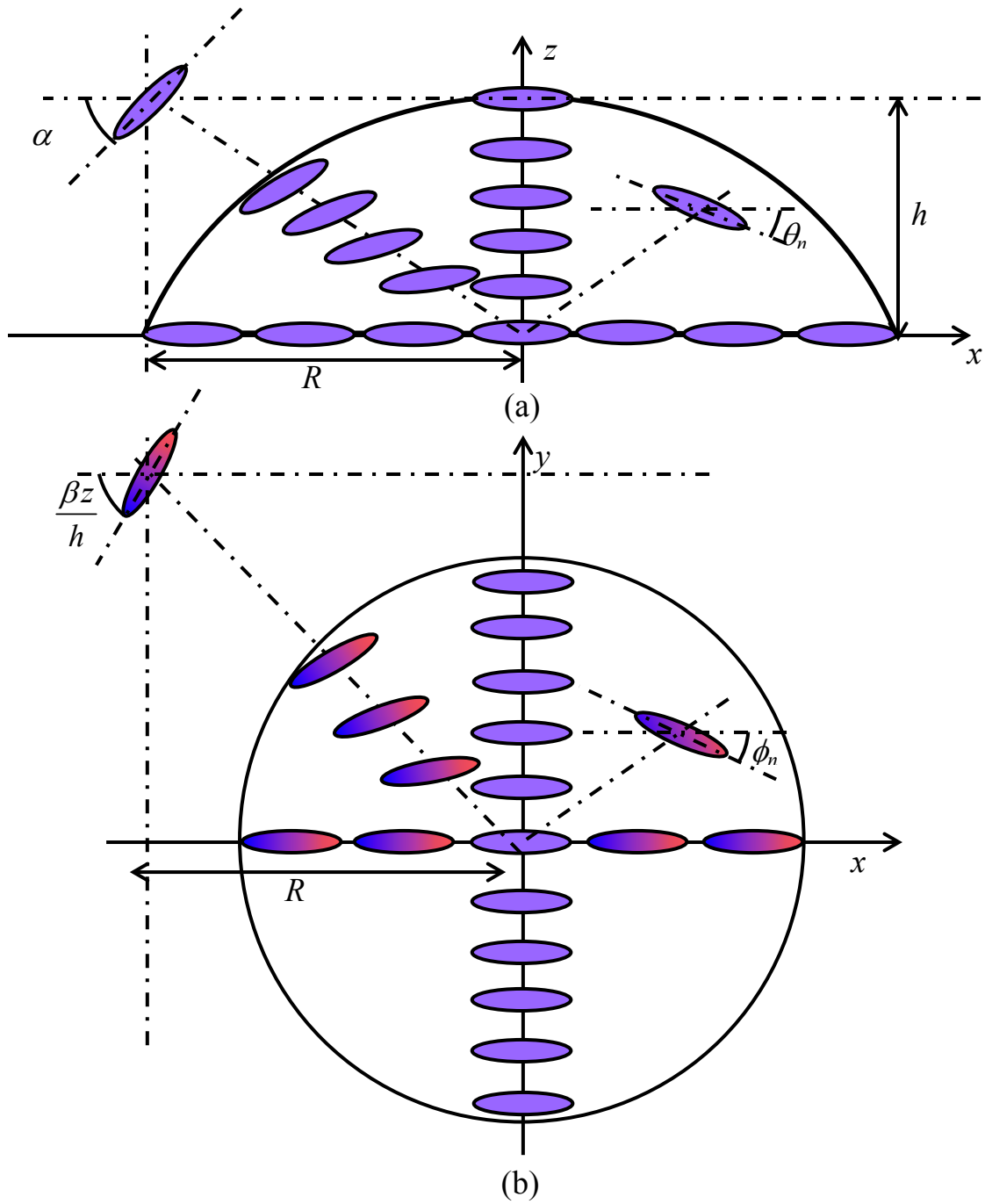
Fig. S1. Schematic illustrations about the parameters in Eq. (3). (a) is the configuration at xz-plane ($y = 0$) and (b) at the plane normal to z axis with $z \neq 0$.
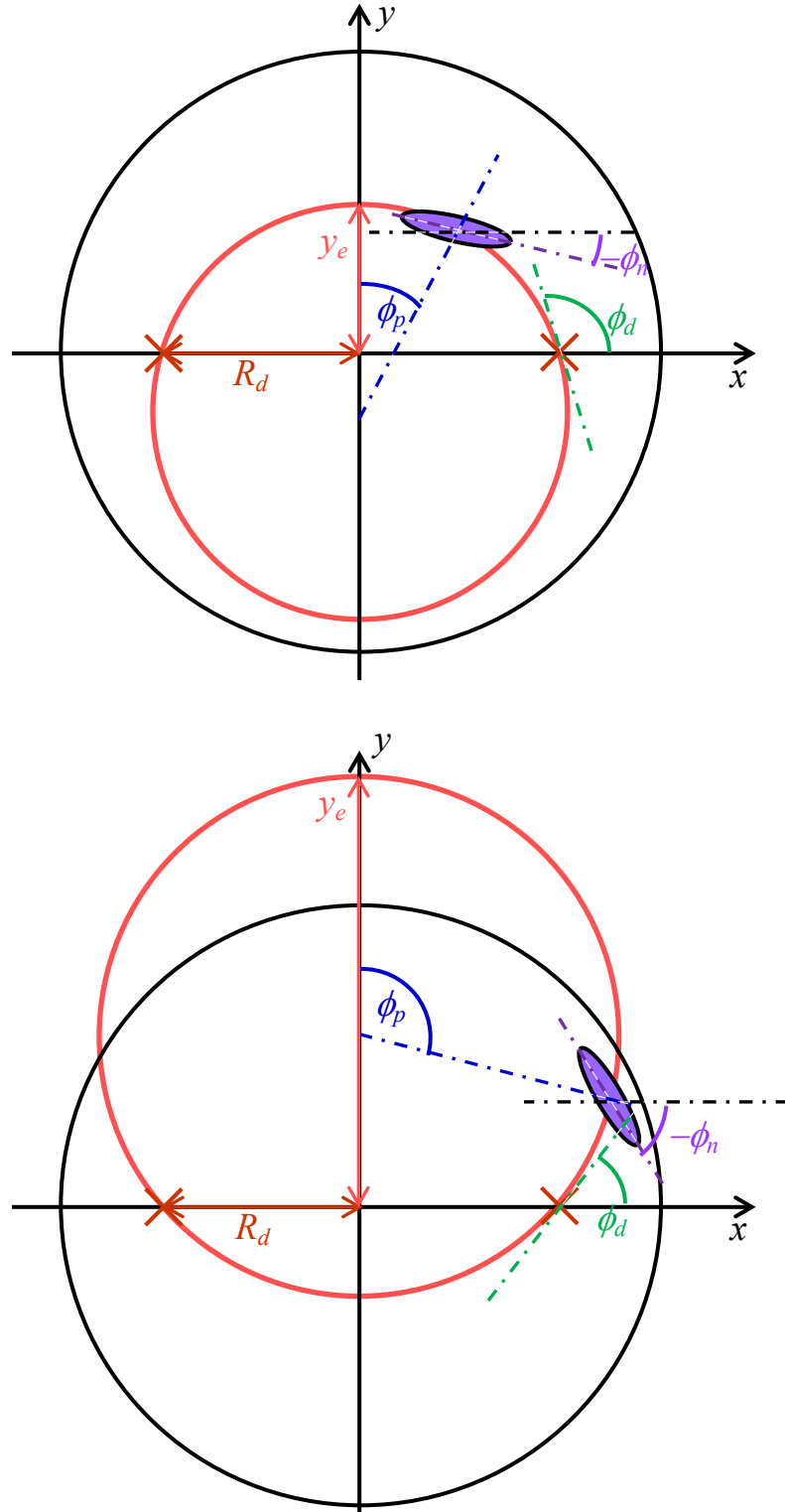
Fig. S2. Schematic illustrations about the parameters in Eq. (2). Both figures show the configuration at the xy-plane ($z = 0$).
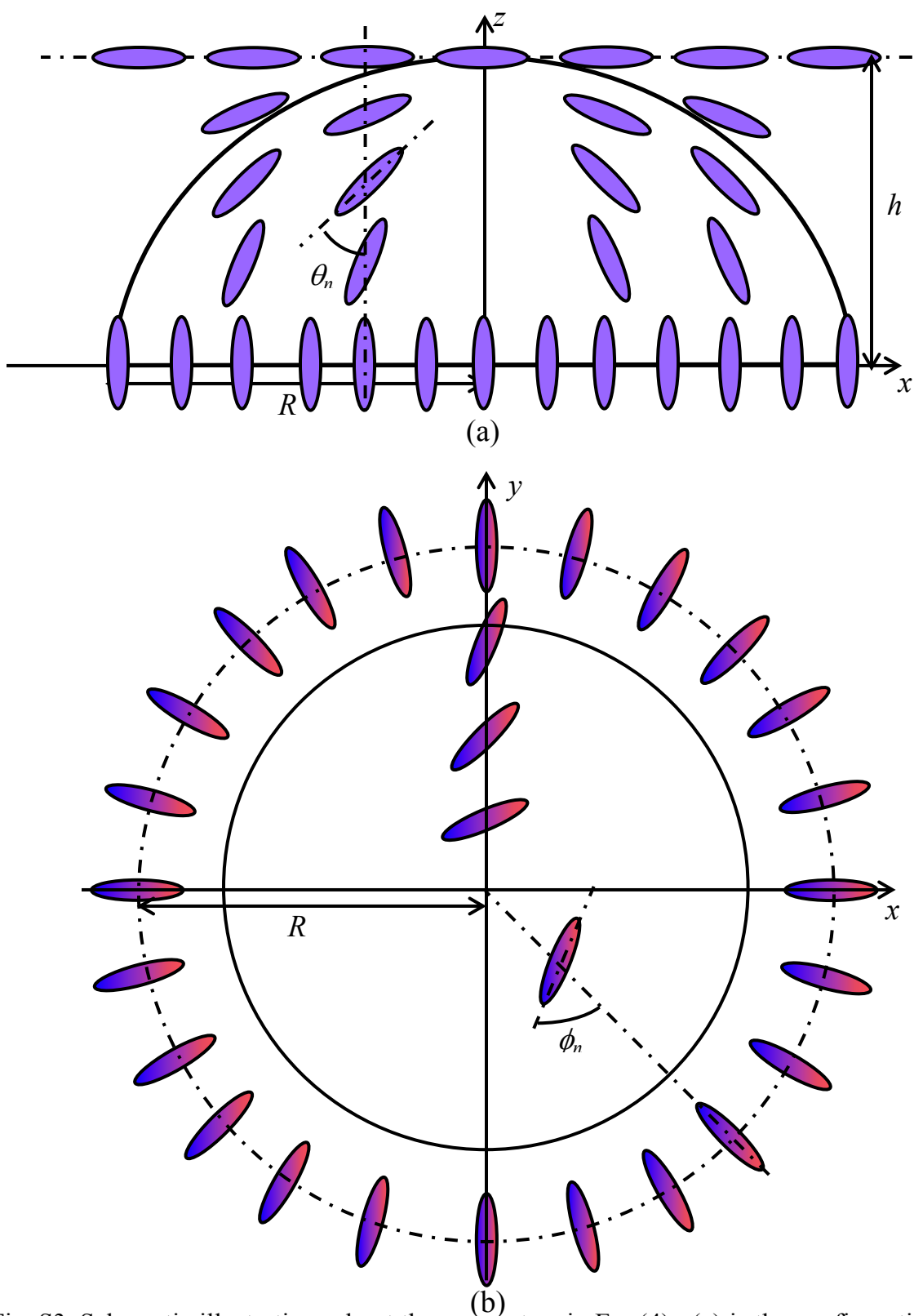
Fig. S3. Schematic illustrations about the parameters in Eq. (4). (a) is the configuration at xz-plane ($y = 0$) and (b) at the plane normal to z axis with $z \neq 0$. In (a), the case for $\beta = 0$ is shown.

**Supplementary Material 3.** Free energy distribution for equal elastic constants ($K_1 = K_2 = K_3$) based on Eqs. (2), (3) and (4). This is equivalent to the distribution of splay, twist and bend deformation rates, which are shown by red, green and blue colours in Fig.S4. (a) and (b) correspond to the energy distribution in the droplet on the bare glass, and they were calculated with $R_d = 0.7R$ and $R$ in Eq. (2), respectively. Large splay deformation is induced around the two point defects in (b), while in (a), the splay is replaced by bend deformation at the surface. Although the splay deformation still exists around the line defects, the total amount of the splay in (a) is decreased from (b). (c) and (d) corresponds to the case of the PVA-coated substrate, and they were calculated at the bottom and the middle plane, respectively.. In this case, the bend deformation is relatively suppressed owing to the strong planar anchoring and low contact angle. (e) and (f) correspond to the case of the homeotropic PI substrate, and they were calculated with $\beta = \pi / 2$ and 0 in Eq. (4), respectively. At the droplet center, splay deformation rate diverges in (f). In (e), on the other hand, the splay is partially replaced by twist and bend deformations, which diverge at the droplet center instead of the splay.
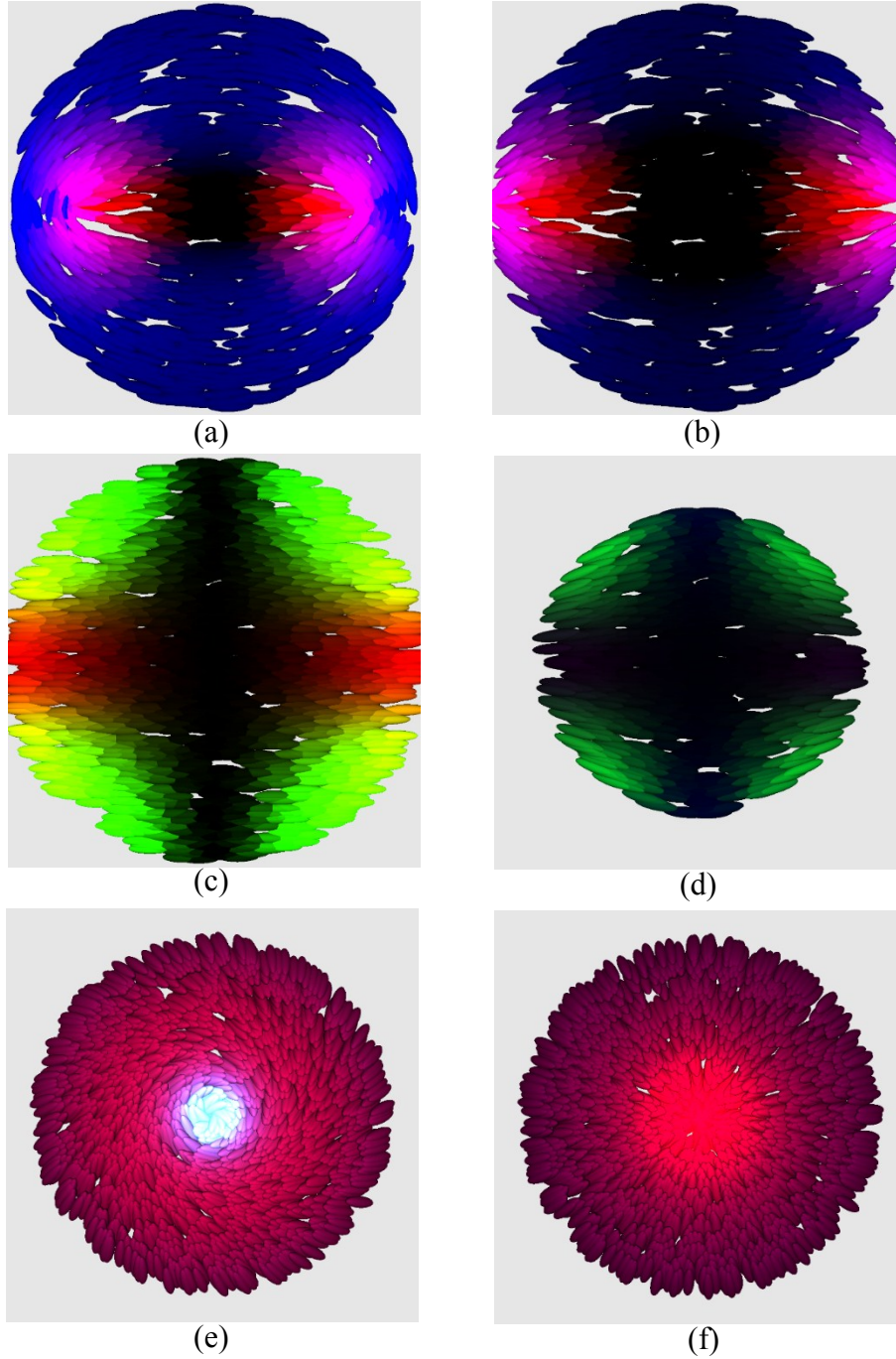
Fig. S4. Free energy distribution for equal elastic constants ($K_1 = K_2 = K_3$). The energy derived from splay, twist and bend deformations are shown by red, green and blue colours, respectively. The calculations were based on Eq. (2) in (a) and (b), Eq. (3) in (c) and (d) and Eq. (4) in (e) and (f). (a), (b) and (c) are the distribution at the substrate, and (d), (e) and (f) at the mid-plane. (a) and (b) correspond to the case of $R_d = 0.7R$ and $R$ in Eq. (2), and (e) and (f) correspond to the case of $\beta = \pi / 2$ and 0 in Eq. (4), respectively.

**Supplementary Material 4.** Estimation of anchoring constant at air-LC interface on the basis of the N droplet on PVA-coated substrate.

The elastic free energy density for the director deformation is described as[62]:

$$f_d = \frac{1}{2}K_1(\mathrm{div}\mathbf{n})^2 + \frac{1}{2}K_2(\mathbf{n}\cdot\mathrm{rot}\mathbf{n})^2 + \frac{1}{2}K_3 \mid \mathbf{n}\times\mathrm{rot}\mathbf{n} \mid^2 - \frac{1}{2}(K_2 + K_{24})\mathrm{div}(\mathbf{n}(\mathrm{div}\mathbf{n}) + \mathbf{n}\times\mathrm{rot}\mathbf{n}) , \quad (S6)$$

where $K_1, K_2, K_3$ and $K_{24}$ are the splay, twist, bend and saddle-splay elastic constants. In addition, the anchoring energy for planar unidirectional anchoring is given as,

$$f_a = \frac{W}{2}\left(1 - (\mathbf{n}\cdot\mathbf{e})^2\right), \quad (S7)$$

where $W$ is the anchoring constant and $\mathbf{e}$ is the unit vector indicating the easy orientation axis. The total free energy for the director field of Eq. (3) in a spherical-cap region can be calculated. Under the approximation that $\alpha \ll 1$, $\beta \ll 1$ and $\theta_c \ll 1$, the free energy is obtained as,

$$F \sim \pi\left[\frac{K_1 R}{12\theta_c}\left(\alpha^2 - \frac{W_{air}R\theta_c^2}{K_1}\alpha\right) + \frac{K_2 R}{96\theta_c}\left(\beta^2 - \frac{4W_{air}R\theta_c^3}{K_2}\beta\right)\right] + \mathrm{const} , \quad (S8)$$

where $W_{air}$ indicates the anchoring constant at air-LC interface. The absence of the anchoring energy at the LC-substrate interface is due to the assumption of the director field: in Eq. (3), since the director completely aligns along the direction of $\mathbf{e}$ at $z = 0$, the corresponding anchoring energy becomes 0. $\alpha$ and $\beta$ are obtained by the minimization of S8:

$$\alpha = \frac{WR\theta_c^2}{2K_1} , \quad (S9a)$$

$$\beta = \frac{2WR\theta_c^3}{K_2} . \quad (S9b)$$

Assuming $\theta_c \sim 0.49\,\mathrm{rad}$ from Table 1, $K_2 \sim 10^{-11} - 10^{-12}\,\mathrm{N}$ from Ref. [62], $\beta \sim 10^0 - 10^{-1}$ and $R \sim 10^{-5}\,\mathrm{m}$, we obtain $W_{air} \sim 10^{-6} - 10^{-8}\,\mathrm{N/m}$ from Eq. (S9b).

More generally, the elastic and the anchoring energies at air-LC interface in all of the N droplets in this paper would be estimated as $F_d \sim KR \sim 10^{-16} - 10^{-17}\,\mathrm{J}$ and $F_a \sim W_{air}R^2 \sim 10^{-16} - 10^{-18}\,\mathrm{J}$. In addition, the anchoring constant of PVA is $W_{PVA} \sim 10^{-5}\,\mathrm{N/m}$ from Ref. [61], and the corresponding energy is estimated as $F_{aP} \sim W_{PVA}R^2 \sim 10^{-15}\,\mathrm{J}$.

**Supplementary Material 5.** The director field and Jones matrix calculation for the droplets with conical alignment on homeotropic PI substrate.

The director field in a spherical-cap nematic droplet on a homeotropic substrate often shows a conical symmetry (Figs. S1(a)-(a″). This director field is described also by the formulation of eq. (3) in the main text, but the factor $\beta$ should be zero, instead of $\beta=\pi/2$ used in the twisted conical director. The computer-generated 3D representation is portraited in Fig. S5(b)-(b″).

POM is simulated by using this conical director field. As shown in Fig. S6, the result shows a usual Maltese-cross like pattern whose extinctions are not twisted at all like the experimental result (Fig. 1(c) and (c′)). The much closer resemblance between Fig. 6a and Fig. 6(a′) clarifies that the present system is not the conventional conical system, but is the twisted conical system as discussed in Section IV-A*(3)* in the main text.

(a)  (b)

(a′)  (b′)

(a″)  (b″)
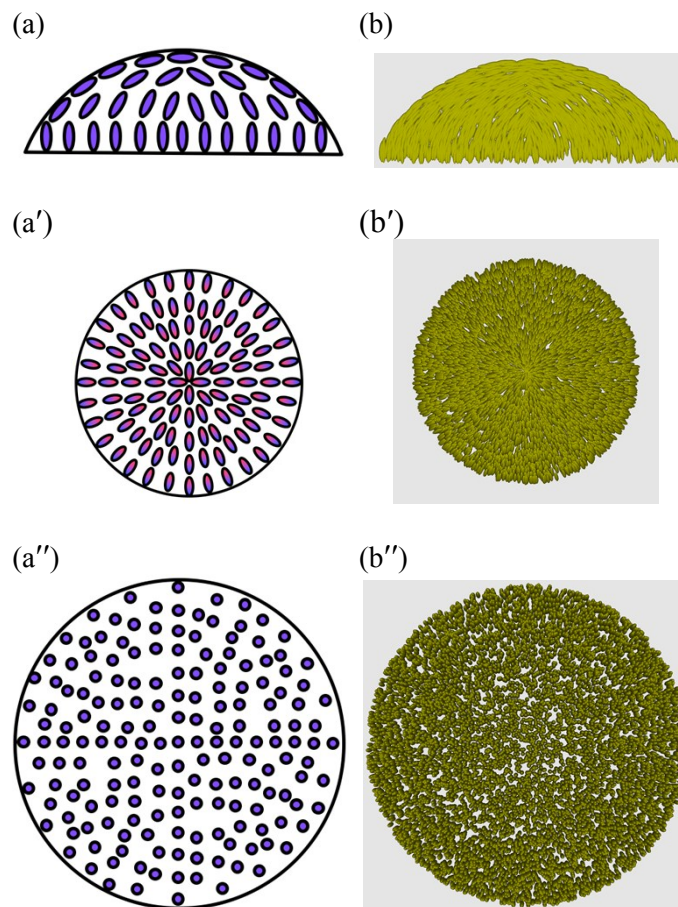
Fig. S5. (a-a″) Schematics and (b-b″) computer-generated 3D cartoons of the conical director field which is often observed in the spherical-cap droplets on the homeotropic surfaces. At (a, b) the vertical mid-plane, (a′, b′) the horizontal mid-plane, and (a″, b″) at the substrate plane.
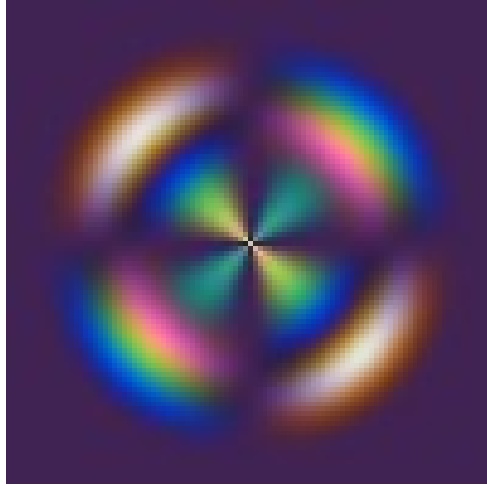
Fig. S6. The simulated POM based on the conventional conical nematic director field given in Fig. S5.

**Supplementary Material 6.**

The schematic illustration for the structural model of the NTB droplet on homeotropic PI-coated substrate is shown in Fig. S7(a). The droplet is separated into the three region of I–III.

**Region I.** Outside of the cylindrical part of region II with the radius of $R_c$. Here, the pseudo-layer structure of $N_{TB}$LC is embedded with a slight deformation as shown by the red curves. Smaller droplets shown by Fig. 2(f) consists of only this region. As shown in Figs. 2(f), (f') and the inset of Fig. 7(c), focal-conic fan texture is observed in region I, which indicates the existence of the deformed layer structure.

**Region II.** Central cylindrical part with the radius of $R_c$. In this region, the pseudo-layer structure with no deformation is considered to be embedded. Thus, elastic free energy should be basically zero in region II in contrast to region I and III. We consider that this energetic advantage would generate the region II for larger droplets.

**Region III**. The spherical-cap part on region II. Its height $h_3$ is estimated to be several hundreds of nanometers as shown in Fig. S7(b). The estimation of $h_3$ was performed with the measurement result of $R_c$ (Fig.7(c)) and the assumption that the droplet shape is a part of a sphere. $h_3$ is given by the following equations:

$$h_3 = R_0 - \sqrt{R_0^2 - R_c^2} ,$$

$$R_0 = \frac{R}{\sin \theta_c} ,$$

where $R$ is the droplet radius and $\theta_c$ the contact angle.

In addition, in region III, $N_{TB}$LC is surrounded by the Region II-III boundary with homeotropic anchoring and the air-LC interface with planar anchoring. Therefore, strong geometrical frustration is induced in this region. Here we considered that such frustration might melt the pseudo-layer of $N_{TB}$LC, so that NLC would be embedded. As shown in Figs. 2(f') and the inset of Fig. 7(c), the texture similar to that of NLC droplet (Fig. 2(c) and (c')) is observed inside the circle with the radius of $R_c$. This supports that the melting of the pseudo-layer of $N_{TB}$LC in region III.
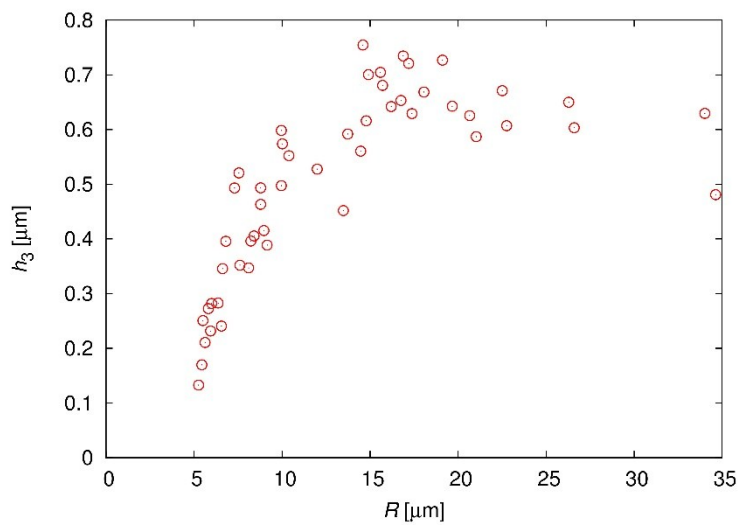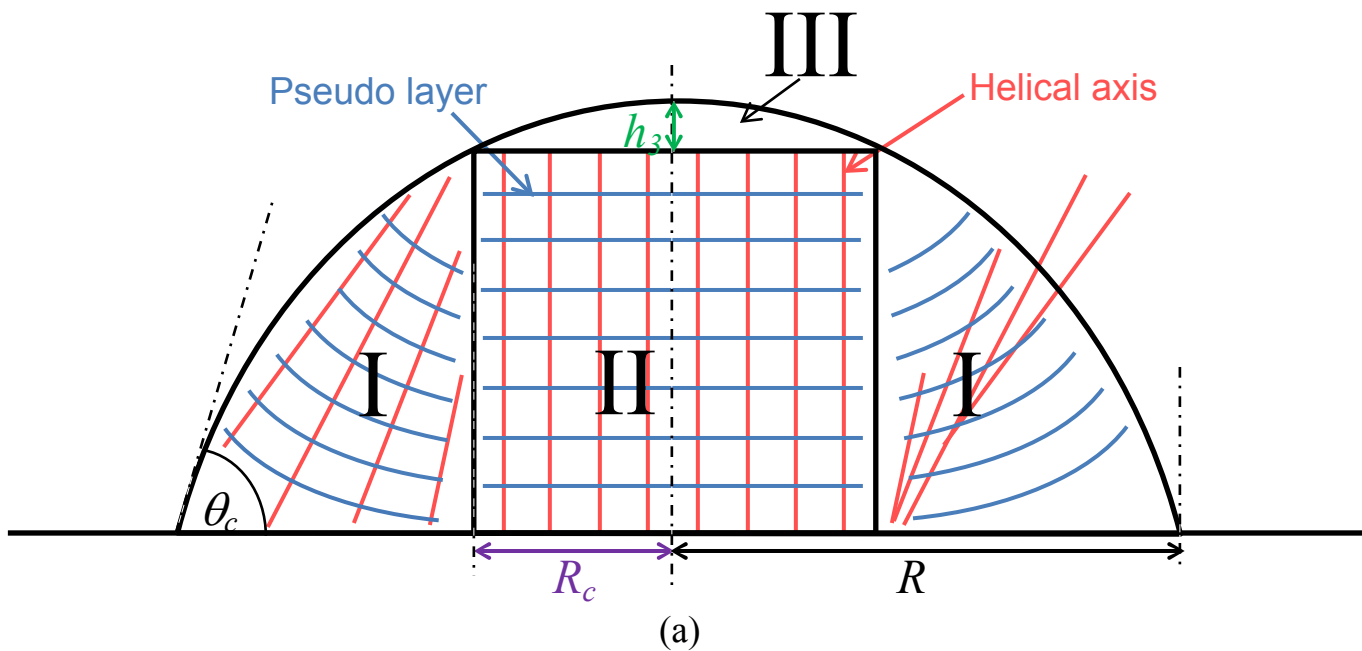
FIG. S7 (a) Schematic illustration for the structural model of the NTB droplet on homeotropic PI-coated substrate. (b) Dependence of the height of region III on droplet radius. In (a), the distribution of the helical axis is illustrated by the red lines, and the pseudo-layer due to the helix formation by the blue lines.